Chapter 2
Optical Frequency Rectification

Sachit Grover and Garret Moddel

Abstract Submicron antenna-coupled diodes, called optical rectennas, can directly rectify solar and thermal electromagnetic radiation, and function as detectors and power harvesting devices. The physics of a diode interacting with electromagnetic radiation at optical frequencies is not fully captured in its DC characteristics. We describe the operating principle of rectenna solar cells using a quantum approach and analyze the requirements for efficient rectification.

In prior work classical concepts from microwave rectenna theory have been applied to the analysis of photovoltaic power generation using these ultra-high-frequency rectifiers. Because of their high photon energy the interaction of petahertz-frequency waves with fast-responding diodes requires a semiclassical analysis. We use the theory of photon-assisted transport to derive the current–voltage [$I(V)$] characteristics of metal/insulator/metal (MIM) tunnel diodes under illumination. We show how power is generated in the second quadrant of the $I(V)$ characteristic, derive solar cell parameters, and analyze the key variables that influence the performance under monochromatic radiation and to a first-order approximation.

The photon-assisted transport theory leads to several conclusions regarding the high-frequency characteristics of diodes. The semiclassical diode resistance and responsivity differ from their classical values. At optical frequencies, a diode even with a moderate forward-to-reverse current asymmetry exhibits high quantum efficiency.

An analysis is carried out to determine the requirements imposed by the operating frequency on the circuit parameters of rectennas. Diodes with low resistance and capacitance are required for the RC time constant of the rectenna

S. Grover (✉)
National Center for Photovoltaics, National Renewable Energy Laboratory,
15013 Denver West Parkway, Golden, CO 80309-0425, USA
e-mail: sachitgrover@ieee.org

G. Moddel
Department of Electrical, Computer, & Energy Engineering, University of Colorado,
Boulder, CO 80309-0425, USA

G. Moddel and S. Grover (eds.), *Rectenna Solar Cells*,
DOI 10.1007/978-1-4614-3716-1_2,

to be smaller than the reciprocal of the operating frequency and to couple energy efficiently from the antenna.

Finally, we carry out a derivation that extends the semiclassical theory to the domain of non-tunneling based diodes, showing that the presented analysis is general and not restricted to the MIM diode.

2.1 Introduction

At low frequencies, rectification is generally associated with AC voltage excitation across a nonlinear element (diode) that leads to generation of a net DC current due to the asymmetry in the diode characteristics. When considering lightwaves, rectification connotes excitation of electron–hole pairs across the bandgap of a semiconductor and their separation leading to generation of a DC current. Optical rectennas are high-frequency elements that extend the concept of rectification of an AC excitation from low frequencies to light waves. The high-frequency operation poses severe requirements on the antenna and diode elements. It also necessitates a quantum-mechanical approach for analyzing the operation of the rectenna [1].

A rectenna consists of an antenna connected to a diode in which the electromagnetic radiation received by the antenna is converted to a DC signal by the diode. Such an arrangement is shown in Fig. 2.1. The conversion from AC to DC occurs due to the difference in resistance of the diode for the positive and the negative cycles of the oscillating current induced on the antenna. Depending on whether the DC signal is sensed by an amplifier or applied across a load resistance, the rectenna can be configured as a detector or as a photovoltaic rectifier.

For microwave frequencies, rectennas with power-conversion efficiencies greater than 90 % have been demonstrated [2] and are used in a variety of energy transmission [3] and harvesting [4, 5] applications. For higher frequencies, detectors based on rectennas have been widely investigated [6]. Photovoltaic rectification using rectennas was originally proposed [7] and patented [8] several decades ago, and has recently gained significant attention [9]. Photovoltaic rectification is still in the research phase. Several components need to come together to enable high efficiency optical rectennas for energy harvesting. Ideally, a low-loss broadband antenna collecting coherent radiation has to be impedance matched to an ultra-high-frequency diode with a large nonlinearity. Several chapters that follow in this book are dedicated to describing these features.

In Sect. 2.2 of this chapter we explain the rectification mechanism of diodes operating at optical frequencies. In Sect. 2.3 we outline the requirements for a rectenna to have efficient rectification. We derive the solar cell characteristics for rectennas in Sect. 2.4. Sections 2.2, 2.3, 2.4 are based on our publications that describe the operating mechanism of optical rectennas [10] and the performance limits for MIM diode based rectennas [11]. In Sect. 2.5 we use the nonequilibrium Green's function (NEGF) formalism to derive the illuminated $I(V)$ characteristics for non-tunneling based diodes. The result of this derivation makes the semiclassical analysis carried out for MIM diodes more generally applicable to any rectifying element.

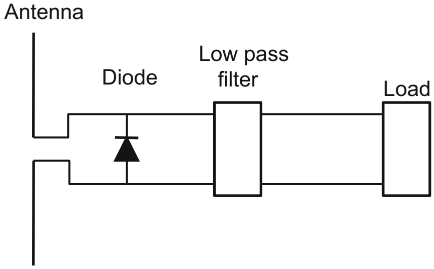

Fig. 2.1 Schematic of an antenna-coupled diode rectifier, also known as a rectenna [© IEEE]

2.2 Diode Characteristics at Optical Frequencies

The choice of a suitable diode for a rectenna is based on its operating frequency. The transit time of charges in semiconductor p-n junction diodes limits their frequency of operation to the gigahertz range [12]. At 35 GHz, rectennas using GaAs Schottky diodes have been designed [13]. Schottky diodes are also used at terahertz and far-infrared frequencies [14, 15]. However, beyond 12 THz the MIM tunnel diode is required to provide a sufficiently fast response for rectennas [16].

The MIM tunnel diode has been a potential candidate for use in optical frequency rectennas as its nonlinearity is based on the femtosecond-fast transport mechanism of quantum tunneling [17, 18]. Even though they have been successfully used in detectors operating at gigahertz [19], the efficiency of MIM-based rectennas has been limited at higher frequencies because of RC time constant limitations [20–22]. Here we use the MIM tunnel diode as an example to facilitate a semiclassical quantum-mechanical derivation for operating characteristics of tunnel diodes at high frequency.

Only at a relatively low frequency can a tunnel diode be considered as a classical rectifier [22]. This frequency is typically in the terahertz range. The rectification is no longer classical if the voltage corresponding to the energy of the incident photons (photon voltage: $V_{\mathrm{ph}} = \hbar\omega/e$) is comparable to or greater than the voltage scale over which curvature in the diode's $I(V)$ curve is significant. For MIM tunnel diodes the nonlinearity is on the scale of a few tenths of a volt while optical frequencies have a photon voltage in the range of 1 V. Therefore, to study rectification at optical frequencies, we use a semiclassical analysis based on photon-assisted tunneling (PAT) [23, 24].

To study the interaction of an optical excitation with electrons tunneling across a barrier, consider an MIM tunnel diode that is biased at a DC voltage of V_{D} and excited by an AC signal of amplitude V_ω and frequency ω. The overall voltage across the diode is

$$V_{\mathrm{diode}} = V_{\mathrm{D}} + V_\omega \cos(\omega t) \tag{2.1}$$

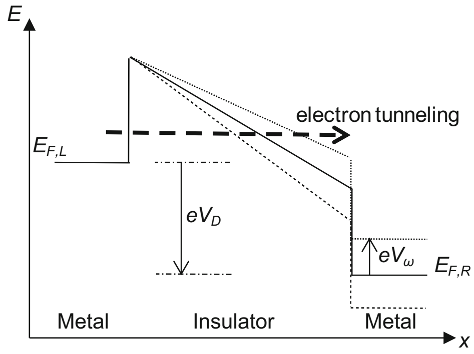

Fig. 2.2 Classical model to account for the applied AC signal that modulates the Fermi level on one side of the tunnel junction [© IOP [10]]

Classically the effect of the AC signal is modeled by modulating the Fermi level on either side of the tunnel junction while holding the other side at a fixed potential, as shown in Fig. 2.2.

Effectively, the low frequency AC signal results in an excursion along the DC $I(V)$ curve around a bias point given by V_D.

For a high-frequency signal, the effect of V_ω is accounted through a time dependent term in the Hamiltonian H for the contact [23], written as

$$H = H_0 + eV_\omega \cos(\omega t) \tag{2.2}$$

where H_0 is the unperturbed Hamiltonian in the contact for which the corresponding wavefunction is of the form

$$\psi(x, y, z, t) = f(x, y, z)\mathrm{e}^{-iEt/\hbar} \tag{2.3}$$

where E is the total energy of electron including the absolute Fermi energy (E_F). The harmonic perturbation in (2.2) leads to an additional phase term whose effect can be modeled with a time dependent term in the wavefunction as

$$\psi(x, y, z, t) = f(x, y, z)\mathrm{e}^{-iEt/\hbar} \exp\left[-(i/\hbar)\int_t dt\prime\, eV_\omega \cos(\omega t\prime)\right] \tag{2.4}$$

Integrating over time and using the Jacobi-Anger expansion, the wavefunction can be written as

$$\psi(x, y, z, t) = f(x, y, z) \sum_{n=-\infty}^{+\infty} J_n\left(\frac{eV_\omega}{\hbar\omega}\right) \mathrm{e}^{-i(E+n\hbar\omega)t/\hbar} \tag{2.5}$$

where J_n is the Bessel function of order n. The modified wavefunction indicates that an electron in the metal, previously at energy E, can now be located at a multitude

Fig. 2.3 An electron at energy E absorbs or emits photons. The transmission probability of the electron increases at higher energies [© IOP [10]]

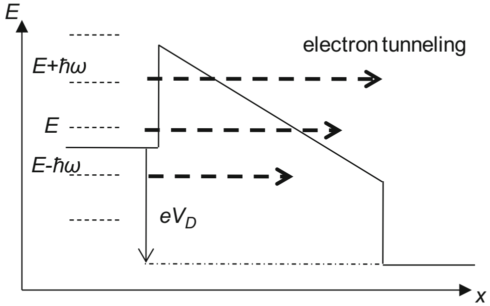

of energies separated by the photon energy ($\hbar\omega$) as shown in Fig. 2.3. The amplitude of the electron being found at energy $E + n\hbar\omega$ is given by the Bessel function of order n, where n corresponds to the number of photons absorbed or emitted by the electron in a multiphoton process. The time dependent wavefunction is normalized since the infinite sum of the square of Bessel terms is unity. The electron density is proportional to the modulus squared of the wavefunction and therefore to the square of the Bessel function.

Heuristically, the effect of the wavefunction modulation on the tunnel current is to modulate all such single-electron states with steps of DC voltage proportional to V_{ph} [24]. Thus in addition to the DC voltage, there is a voltage nV_{ph} that is applied across the diode with a weighting factor $J_n^2(\alpha)$, where $\alpha = eV_\omega/V_{\mathrm{ph}}$. The DC current under illumination is then given by

$$I_{\mathrm{illum}}(V_{\mathrm{D}}, V_\omega) \sum_{n=-\infty}^{\infty} J_n^2(\alpha) I_{\mathrm{dark}}(V_{\mathrm{D}} + nV_{\mathrm{ph}}) \tag{2.6}$$

where $I_{\mathrm{dark}}(V)$ is the tunnel current in the un-illuminated diode.

We use (2.6) in Sect. 2.4 to study the solar cell characteristics of rectennas.

The above derivation is based on MIM tunnel diodes. In Sect. 2.5, we derive a generalized theory for optical rectification that extends the applicability of (2.6) to the more general case of any mesoscopic diode operating at high frequency.

Here we limit the analysis to include illumination at a single frequency. Characteristics of a diode illuminated by several frequencies are given in Chap. 3.

In the remaining part of this section, we discuss the ramifications of single-frequency PAT on diode resistance and nonlinearity at optical frequencies. The importance of the diode responsivity is discussed in Sect. 2.3.1.

Apart from the DC component of the tunnel current given by (2.6), there is a time-dependent current that consists of the harmonics of ω that is given by [25]

$$I_\omega = \sum_{n=-\infty}^{\infty} J_n(\alpha)[J_{n+1}(\alpha) + J_{n-1}(\alpha)]\, I_{\mathrm{dark}}(V_{\mathrm{D}} + nV_{\mathrm{ph}}) \tag{2.7}$$

Combining (2.6) and (2.7), we obtain the semiclassical diode resistance (R_D^{SC}) and the semiclassical diode responsivity (β_i^{SC}) using the equations [24]

$$R_D^{SC} = \frac{V_\omega}{I_\omega}, \quad \beta_i^{SC} = \frac{\Delta I}{\frac{1}{2} V_\omega I_\omega} \tag{2.8}$$

where the superscript SC denotes the use of the semiclassical PAT formulation. The ΔI is the incremental DC current due to the illumination and is given by $\Delta I = I_{illum} - I_{dark}$.

From here on we simplify the analysis by assuming $\alpha \ll 1$ such that Bessel function terms only up to first order in n are required. This implies a small probability for multiple photon emission or absorption. One can mathematically verify that higher order terms are negligible for $\alpha \ll 1$ by using the approximation for Bessel functions $J_0(\alpha) \approx 1 - \alpha^2/4$ and $J_{\pm n}(\alpha) \approx (\pm\alpha/2)^n/(n!)$. This gives the ratio of $J_{n+1}/J_n = \alpha/(n+1)$ implying sharply decreasing contribution with increasing n at small α. From (2.7), to first order in $n(=-1, 0, 1)$, R_D^{SC} is given by [25]

$$R_D^{SC} = \frac{2V_{ph}}{I_{dark}(V_D + V_{ph}) - I_{dark}(V_D - V_{ph})} \xrightarrow{\text{classical}} \frac{1}{I'} \tag{2.9}$$

which in the classical limit ($\hbar\omega \to 0$) leads to the differential resistance. We note that the semiclassical resistance is the reciprocal of the slope of a secant between two points in the $I(V)$ curve separated by $2V_{ph}$ rather than the tangential slope at a single point for the classical case.

The semiclassical responsivity is similarly found from the first-order approximation of (2.6) and (2.7), and is given by [25]

$$\beta_i^{SC} = \frac{1}{V_{ph}} \left[\frac{I_{dark}(V_D + V_{ph}) - 2I_{dark}(V_D) + I_{dark}(V_D - V_{ph})}{I_{dark}(V_D + V_{ph}) - I_{dark}(V_D - V_{ph})} \right] \xrightarrow{\text{classical}} \frac{1}{2} \frac{I''}{I'} \tag{2.10}$$

In the limit of small photon energies this leads to the classical formula for responsivity given by 1/2 the ratio of second derivative of current to the first derivative.

Classically, the diode resistance and responsivity are independent of frequency. The semiclassical resistance and responsivity deviate from the classical values at high photon energies. In Fig. 2.4 we plot the semiclassical resistance and responsivity at zero bias vs. the photon energy ($\hbar\omega$) for a simulated diode $I(V)$ [11]. As the photon energy increases, the resistance of the diode decreases and the responsivity decreases. For large $\hbar\omega$ the responsivity approaches the limit of $e/\hbar\omega$, which is the maximum achievable responsivity corresponding to one electron per photon. Therefore, even a diode with poor quantum efficiency at low $\hbar\omega$ becomes more efficient and thus adequate at high $\hbar\omega$.

In the next section, we discuss the impact of the semiclassical diode parameters on the rectification efficiency and impedance matching with the antenna.

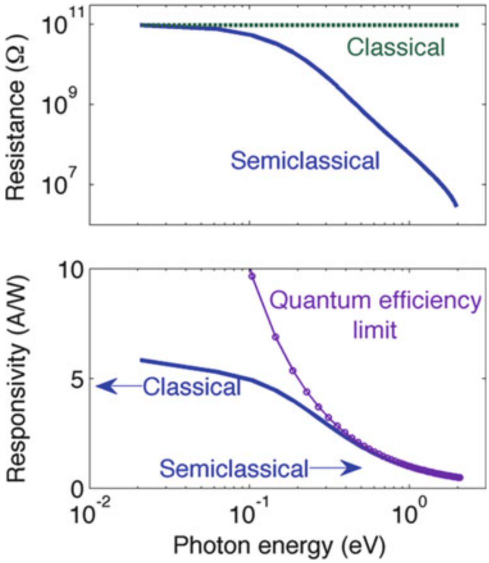

Fig. 2.4 Variation of classically and semiclassically calculated resistance and responsivity vs. photon energy at $V_D = 0$ V. As the photon energy increases, the semiclassical resistance becomes significantly lower than the classical value and the semiclassical responsivity approaches the value corresponding to unity quantum efficiency [© IEEE [11]]

2.3 Rectenna Requirements

2.3.1 Overview

The rectification efficiency (η) of a rectenna is determined by the combination of several factors as given in (2.11) [26]. The efficiency (η) is not the same as the conventionally accepted efficiency of a solar cell. Rather this is closer in definition to the quantum efficiency or spectral response of a solar cell that provides the short-circuit current produced for a given amount of input AC power. The overall cell efficiency for rectenna solar cells is derived in Chap. 3.

$$\eta = \eta_a \eta_s \eta_c \eta_j \tag{2.11}$$

where

- η_a is the efficiency of coupling the incident EM radiation to the antenna and depends on the radiation pattern of the antenna as well as its bandwidth. Another consideration for η_a that is important for energy harvesting is the area over which radiation received from the source (e.g., sun) is coherent and can be captured by a single antenna element. For the case of the sun, the coherence radius is a few 10's of microns. Chapter 4 gives a comprehensive study of this criterion.
- η_s is the efficiency with which the collected energy propagates to the junction of the antenna and the diode and is largely governed by losses in the antenna, such as resistive loss at high frequencies. For a more detailed description of antenna efficiency, the reader is referred to Chaps. 11, 12, and 13.

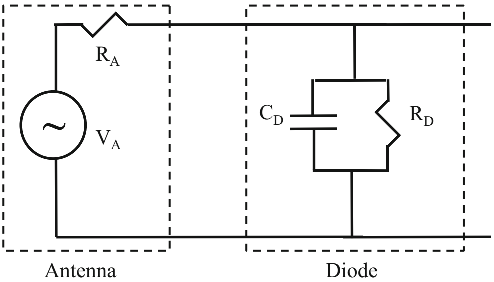

Fig. 2.5 A small signal circuit representation of the rectenna for determining the antenna-to-diode coupling efficiency [11]. The antenna is modeled as a voltage source in series with a resistance and the MIM diode is modeled as a resistor in parallel with a capacitor [© IEEE [11]]

- η_c is the coupling efficiency between the antenna and the diode and requires the antenna and the diode to be impedance matched for efficient power transfer. Series resistance losses in the diode also need to be considered. We elaborate on impedance matching in Sect. 2.3.2.
- η_j is the efficiency of rectifying the power received in the diode. The efficiency of the diode junction can be expressed in terms of its current responsivity $\eta_j = \beta_i$.

The η_j sets the overall units of η to be A/W implying the DC current produced per watt of incident radiation. An underlying assumption in the above discussion is that the diode has a low RC time constant and an intrinsically high speed. The low RC time constant is needed to ensure that the AC excitation across the diode is not shorted out due to a large diode capacitance. As we derive next, this requirement imposes a frequency limitation on rectennas, different from the requirement for high-speed transport of the charges.

2.3.2 Impedance Matching and RC Cutoff

The antenna-to-diode power-coupling efficiency (η_c) is given by the ratio of the AC power delivered to the diode resistance to the power sourced by the antenna. This ratio can be calculated from the analysis of a circuit of the rectenna shown in Fig. 2.5. The antenna is modeled by a Thévenin equivalent and the diode by the parallel combination of a capacitor and a voltage-dependent resistor. For simplicity of analysis, series resistance of the diode [13] and reactance of the antenna are assumed to be negligible.

The power-coupling efficiency at a frequency ω is given by [20]

$$\eta_c = \frac{P_{\mathrm{AC},R_D}}{P_A} = \frac{4\frac{R_A R_D}{(R_A+R_D)^2}}{1+\left(\omega\frac{R_A R_D}{(R_A+R_D)}C_D\right)^2} \tag{2.12}$$

where $P_A = V_A^2/(8R_A)$. In the above equation, the numerator gives the impedance match between the antenna and the diode with $R_A = R_D$ leading to efficient power transfer.

In Fig. 2.5, if the capacitive branch is open-circuit due to a small capacitance or low frequency, the circuit is essentially a voltage divider between R_A and R_D. The denominator in (2.12) determines the cutoff frequency of the rectenna, which is based on the RC time constant determined by the resistance in parallel with antenna the diode resistance and capacitance. Above the cutoff frequency, the capacitive impedance of the diode is smaller than the parallel resistance, leading to inefficient coupling of power from the antenna to the diode resistor.

As stated earlier, the responsivity form of the overall efficiency (η) indicates the DC current generated normalized to 1 W of incident radiation. In a PV rectifier, the performance measure of interest is the power-conversion efficiency (η_{load}) which is given by the ratio of the DC power delivered to the load and the incident AC power

$$\eta_{load} = \frac{P_{load}}{P_A} = \frac{I_{DC,load}^2 R_{load}}{P_A} \tag{2.13}$$

The $I_{DC,load}$ is proportional to the square of DC current dissipated in the load implying [22]

$$\eta_{load} \propto \beta_i^2 P_A \eta_c^2 \tag{2.14}$$

Keeping aside the antenna efficiency components, the power-conversion efficiency depends on four factors: the diode responsivity, the strength of the AC signal that depends on the power received by the rectenna, the impedance match between the antenna and the diode, and the RC time constant of the circuit.

Efficient coupling of power from the antenna to the diode requires impedance matching between them. Moreover, having a small RC time constant for the circuit implies that the product of the antenna resistance (R_A) in parallel with the diode resistance (R_D) and the diode capacitance (C_D) must be smaller than $1/\omega$ for the radiation incident on the rectenna. This ensures that the signal from the antenna drops across the diode resistor (R_D) and is not shorted out by C_D. Therefore the conditions of $R_D = R_A$ and $\omega(R_A \| R_D)C_D \ll 1$ lead to a unity coupling efficiency, as can be seen from (2.12). The parameters that can be varied to achieve these conditions are the diode area, the antenna resistance, and the composition of the diode. Obtaining a sufficiently low diode resistance to match the antenna impedance is a challenge, and so for this analysis we choose the Ni/NiO (1.5 nm)/Ni MIM diode, which has an extremely low resistance and was used in several high-frequency rectennas [6, 27, 28].

Typical antenna impedances are on the order of 100 Ω [6]. We choose a nominal antenna impedance of 377 Ω, but as will become apparent a different impedance would not help. We vary the diode area, which changes the diode resistance and capacitance. In Fig. 2.6, we show the $\eta_{coupling}$ vs. the diode edge length for a

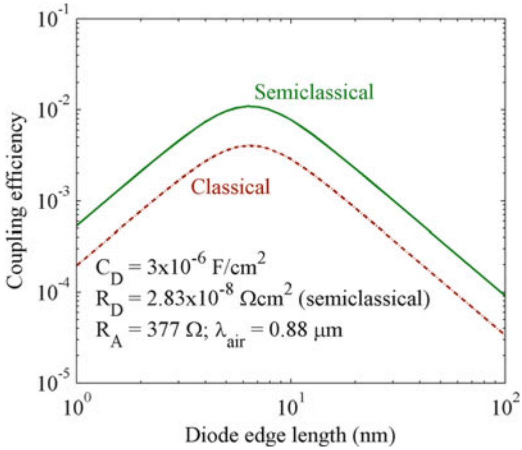

Fig. 2.6 Effect of varying the edge length (for a square diode area) on the antenna-to-diode coupling efficiency [11]. The peak in efficiency is due to the tradeoff between impedance match and cutoff frequency. A simulated $I(V)$ curve is used to calculate the resistance of the Ni–NiO (1.5 nm)–Ni diode using the classical and the semiclassical ($E_{ph} = 1.4$ eV, $\lambda_{air} = 0.88$ μm) forms of (2.9). The barrier height of Ni–NiO is 0.2 eV [28] [© IEEE [11]]

classically and semiclassically calculated diode resistance. The semiclassical resistance, which results from a secant between two points on the $I(V)$ curve, is lower than the classical resistance, as shown in Fig. 2.6, and gives a higher $\eta_{coupling}$. The peak in both the curves occurs at the same edge length, and is an outcome of the balance between the needs for impedance matching and low cutoff frequency.

The coupling efficiency is limited by the combined effect of impedance matching given by the numerator (ideally $R_D/R_A = 1$) and cutoff frequency given by the denominator (ideally $\omega(R_A \| R_D)C_D = 0$) in (2.12). Unity coupling efficiency under the ideal conditions occurs for different edge lengths, as shown in Fig. 2.6a. The overall efficiency is given by the smaller of the two values, limited by the two curves in Fig. 2.7a, which leads to the peak in Fig. 2.6. Increasing the diode resistance 10 times lowers the coupling efficiency by the same factor.

The tradeoff between impedance match to the antenna, for which a small R_D is desired, and a high cutoff frequency, for which a small C_D is desired, is fundamental for parallel-plate devices. Varying the antenna impedance results in a simple translation of both curves in tandem such that the diode edge length for peak efficiency changes as shown in Fig. 2.7a. With an increase in antenna impedance a higher R_D can be accommodated, allowing the diode area to be smaller, and resulting in a desirable smaller C_D. However, the higher R_A also increases the $(R_A \| R_D)C_D$ time constant.

The condition under which the constraints simultaneously lead to a high coupling efficiency is obtained by combining

$$\omega(R_A||R_D)C_D \ll 1 \quad \text{and} \quad \frac{R_D}{R_A} = 1 \Rightarrow R_D C_D \ll \frac{2}{\omega} \tag{2.15}$$

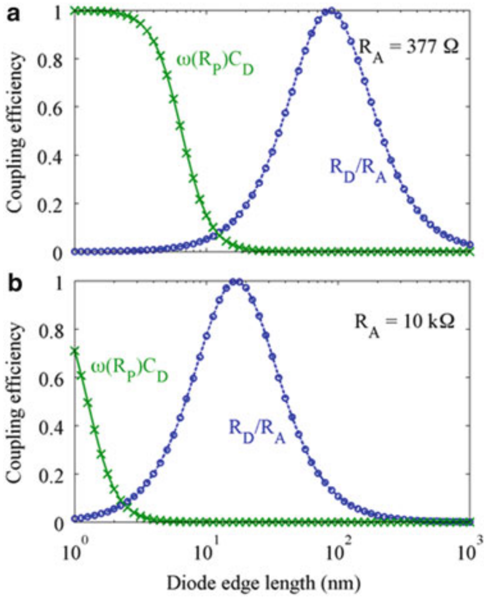

Fig. 2.7 Antenna-to-diode coupling efficiency as a function of diode edge length. The effect of impedance match is separated from cutoff frequency for two antenna impedance values: (**a**) $R_A = 377\ \Omega$, and (**b**) $R_A = 10\ k\Omega$. The parallel combination of R_A and R_D is denoted by R_P. The curves labeled R_D/R_A show the coupling efficiency when only the impedance match is the limiting factor and those labeled $\omega R_P C_D$ show the coupling efficiency when only the cutoff frequency is the limiting factor. The maximum efficiency occurs for an edge length at the small peak where the two curves coincide [© IEEE [11]]

For the model Ni–NiO–Ni diode discussed above, this condition is not satisfied for near-IR frequencies ($\lambda = 0.88$ μm), where $2/\omega = 9.4 \times 10^{-16}$ s is much smaller than $R_D C_D = 8.5 \times 10^{-14}$ s. It is satisfied for wavelengths greater than 80 μm.

Due to the parallel-plate structure of the MIM diodes, the $R_D C_D$ time constant is independent of the diode area and is determined solely by the composition of the MIM diode. As already noted, the Ni/NiO/Ni diode is an extremely low resistance diode and NiO has a small relative dielectric constant (ε_r) of 17 at 30 THz. Even if one could substitute the oxide with a material having comparable resistance and lower capacitance (best case of $\varepsilon_r = 1$), the $R_D C_D$ would still be off by an order of magnitude for near-IR operation. Putting practicality aside completely, a near-ideal resistance would result from a breakdown-level current density of 10^7 A/cm^2 at, say, 0.1 V, giving a resistance of $10^{-8}\Omega$-cm^2. A near-ideal capacitance would result from a vacuum dielectric separated by a relatively large 10 nm, giving a capacitance of ~10^{-7} F/cm^2. The resulting $R_D C_D$ would be ~10^{-15} s, again too large for efficient coupling at visible wavelengths.

For coupling, the relevant resistance is the differential resistance rather than the absolute resistance. A highly nonlinear diode with a sharp turn-on at a positive voltage would therefore give a lower resistance than what we have calculated above. Alas, this does not help at optical frequencies because the differential resistance in the semiclassical case is the inverse of the slope of the secant between points that are $\hbar\omega/e$ above and below the operating voltage. At the large $\hbar\omega$ of optical frequencies the secant mutes the effect of a sharp turn in the $I(V)$ characteristics.

Several techniques are being investigated to overcome the RC constraint and include variations on MIM diodes as well as completely new diode structures. The coupling efficiency of MIM-diode rectennas is improved at longer wavelengths, where the condition imposed by (2.15) is easier to meet. The $R_D C_D$ can also be artificially reduced by compensating the capacitance of the MIM diode with an inductive element, but this is difficult to achieve over a broad spectrum. In Chap. 7, a sharp tip MIM diode is described that can potentially reduce the capacitance while maintaining a low resistance. A design that can circumvent the restrictions imposed on the coupling efficiency is the MIM traveling-wave rectifier [21, 29]. Akin to a transmission line where the geometry determines the impedance, the distributed RC enhances the coupling between the antenna and the traveling-wave structure. However, losses in the metallic regions of the waveguide limit its efficiency as the frequency approaches that of visible light.

A new type of diode called the geometric diode is described in Chap. 10 and can potentially satisfy the requirements of low resistance and capacitance. It rectifies based on a nanoscale asymmetry in the shape of the conducting material that leads to a preferential direction for flow of charge carriers. The absence of a tunneling barrier leads to an extremely low resistance. The planar structure of the geometric diode lifts the capacitance constraint imposed by the parallel-plate structure of the MIM diode.

2.4 Operation at Optical Frequency

In this section we use the PAT theory developed in Sect. 2.2 to derive the illuminated $I(V)$ characteristics of ideal diodes, i.e., for the case of an illuminated rectenna. The power-generating regime is shown to occur in the second quadrant of the $I(V)$ curve. We assume that a constant AC voltage is applied across the diode as the DC bias voltage is varied. This assumption helps to develop the understanding of how an illuminated $I(V)$ curve can be obtained starting with dark $I(V)$ using (2.6). In practice, the magnitude of the AC voltage would vary with the DC bias as explained and dealt with in Chap. 3. Due to the dependence of the diode resistance on AC voltage as given by (2.9), the two assumptions lead to significantly different shapes of the illuminated $I(V)$ curves.

Using the first-order approximation of (2.6), corresponding to $\alpha \ll 1$, the current under illumination can be expressed as

$$I_{\text{illum}}(V_D) = \left(1 - \frac{\alpha^2}{4}\right)^2 I_{\text{dark}}(V_D) + \frac{\alpha^2}{4}\left(I_{\text{dark}}(V_D + V_{\text{ph}}) + I_{\text{dark}}(V_D - V_{\text{ph}})\right) \quad (2.16)$$

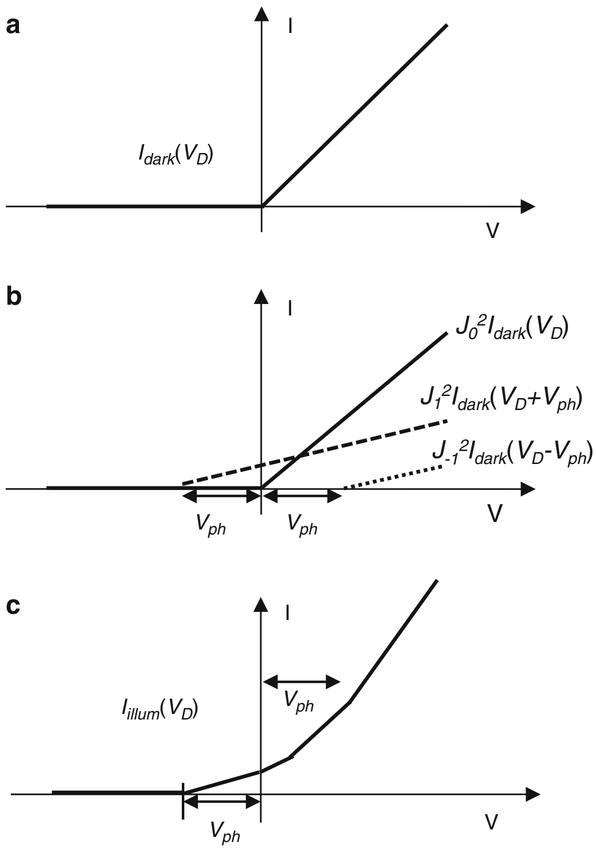

Fig. 2.8 (**a**) Piecewise linear dark $I(V)$ curve. (**b**) Scaled and voltage-shifted components of I_{illum} as given by (2.16) under the assumption of constant AC input voltage. (**c**) Illuminated $I(V)$ curve obtained by adding the components in (**b**). The region of positive current at negative voltage corresponds to power generation [© IOP [10]]

with the first term on the right-hand side representing the dark current due to electrons that are in the unexcited state. The second and third terms represent the current resulting from electrons that undergo a net absorption or emission of a photon, respectively, together denoted as ΔI. To understand the effect of ΔI on I_{illum}, consider an ideal diode with the piecewise linear I_{dark} shown in Fig. 2.8a. As shown in Fig. 2.8b, the two terms in ΔI modify I_{dark} such that a positive current can flow even at zero or a negative DC bias. The sum of the three current components of (2.16) is shown in Fig. 2.8c with power generation occurring in the second-quadrant operation of the diode (in contrast to the fourth-quadrant for a conventional solar cell). The DC current generated depends on V_ω via α and thereby the strength of the illumination and the antenna design.

In the illuminated $I(V)$ curve shown in Fig. 2.8c the voltage-intercept is marked as V_{ph}, which signifies the maximum negative voltage at which a positive current is possible. This occurs for a diode with a high forward-to-reverse current ratio.

As seen in the second quadrant of Fig. 2.8c, the triangular illuminated $I(V)$, under the assumption of constant V_ω, incorrectly suggests a peak efficiency of only 25 %. In Chap. 3, we show that the maximum theoretical efficiency for rectification of monochromatic illumination is 100 %.

2.5 Optical Frequency Rectification in Mesoscopic Diodes

In the semiclassical analysis for the optical response of an MIM diode presented in Sect. 2.2, the $I(V)$ characteristics under illumination are obtained from the DC dark $I(V)$ curve of the diode. To make the operating mechanism of optical rectennas, derived in the previous section, valid for a broader class of diodes a derivation similar to the Tien and Gordon approach [23], but generalized to be applicable even to a non-tunneling based device, is required. Such a theory is presented here [1] and is applicable, for example, to the geometric diode described in Chap. 10.

A mesoscopic junction is categorized as having length-scales comparable to the electron phase coherence length [30]. An asymmetric mesoscopic junction can show rectification due to interaction of carriers with the conductor boundaries. Rectification in such junctions was predicted to occur due to an asymmetric conductor or an asymmetric illumination in a symmetric conductor [31]. At least one of these two conditions is necessary. Photovoltaic effect has been observed in small conductors having geometric asymmetry due to disorder [32] or patterned asymmetric shapes [1].

Platero and Aguado [33] have reviewed several techniques that can be used to study photon-assisted transport in semiconductor nanostructures. Other than Tien and Gordon's approach, all the analyses culminate in a form requiring numerical computation of the transport mechanism, and do not provide insights into the optical behavior through a simple extension of the DC characteristics.

The simplicity of the Tien and Gordon formulation comes with the drawback that the theory is not gauge-invariant. Another limitation of this method is that it does not account for charge and current conservation. To ensure conservation, an AC transport theory such as the one that solves the NEGF and Poisson equations self-consistently [34] is required. In a geometric diode, the dependence of the transport properties on the geometry adds to the complexity.

Here we use the NEGF formulation to derive an equation analogous to Tien and Gordon's equation given by (2.6) but also applicable to an illuminated mesoscopic junction. Starting with the Hamiltonian that describes the material and the structure of the geometric diode, the NEGF approach is used to model geometry-dependent transport, and interaction of electrons with an AC voltage.

Several approximations are made to enable an analytical relation between the DC and illuminated characteristics. Even though these approximations limit the region of applicability of the result, it is nevertheless helpful in understanding the illuminated characteristics of mesoscopic junctions.

2.5.1 Mesoscopic Junction Under Illumination

The starting point for the derivation is the NEGF theory for an illuminated junction given by Datta and Anantram [35]. In this section we reproduce and explain some of their results.

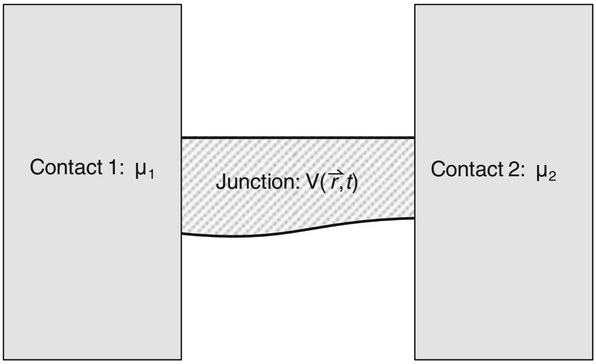

Fig. 2.9 A two terminal device with an arbitrary shape, subjected to an AC potential $V(\vec{r},t)$

Consider a mesoscopic junction connected to two contacts, as shown in Fig. 2.9. It is assumed that charge transport from one contact to the other occurs phase-coherently, and the coherence is broken only by scattering in the contacts. Here, the contacts refer to charge reservoirs, much larger than the device region, held at a fixed potential. Electrons gain or lose energy through scattering in the contacts. The interaction of charge carriers with photons occurs in the device region through a time-varying potential $V(\vec{r},t)$. This interaction, even though inelastic (changes the energy of charge particles), does not cause phase incoherence.

The energy-domain version of Schrödinger's equation for the device in the absence of illumination is [35]

$$\begin{aligned}&\left[E+\tfrac{\hbar^2\nabla^2}{2m}-V_S(\vec{r})+\tfrac{i\hbar}{2\tau_\varphi(\vec{r},E)}\right]G_0^R(\vec{r},E;\vec{r}',E')=\delta(\vec{r}-\vec{r}')\delta(E-E')\\ &\Rightarrow H_0(\vec{r},E)G_0^R(\vec{r},E;\vec{r}',E')=\delta(\vec{r}-\vec{r}')\delta(E-E')\end{aligned} \tag{2.17}$$

where G_0^R is the retarded Green's function that represents the impulse response of Schrödinger's equation. The subscript '0' refers to the Green's function for the un-illuminated case. The wavefunction at any energy E can be obtained from G_0^R. V_s is the static potential in the device. The τ_φ is the scattering (phase-breaking) time in the contacts.

The current in the device is obtained as

$$I=e\hbar\int dE\int dE'\int d\vec{r}\int d\vec{r}'[t_{21}(E,E')f_1(E')-t_{12}(E',E)f_2(E)] \tag{2.18}$$

where f_1 and f_2 are the Fermi-Dirac distributions in contact 1 and 2 respectively. The $t_{21}(E,E')$ is the transmission from an input energy mode E' in contact 1 to an output energy mode E in contact 2, and is given by

$$t_{21}(E,E')=\frac{\hbar}{\tau_{avg}}\iint\limits_{\substack{\vec{r}\in\text{contact1}\\ \vec{r}'\in\text{contact2}}} d\vec{r}d\vec{r}'\,\frac{|G^R(\vec{r},E;\vec{r}',E')|^2}{4\pi^2\tau_\varphi(\vec{r},E)\tau_\varphi(\vec{r}',E')} \tag{2.19}$$

The τ_{avg} is the time over which the current or the transmission is averaged to find the DC component. The un-illuminated case is obtained by replacing G^{R} by G_0^{R} in (2.19).

Equation (2.18) is different from the usual form for the transport equation that takes into account the exclusion principle by counting the filled states on one contact and the empty states on the other. The applicability of this equation for phase-coherent transport is explained by Landauer [36] and the equation is explicitly derived by Datta and Anantram [35].

Under illumination, the Schrödinger equation is modified as [35, 37]

$$\begin{aligned} H_0(\vec{r},E)G^{R}(\vec{r},E;\vec{r}',E') &= \delta(\vec{r}-\vec{r}')\delta(E-E') \\ &+ \sum_{\omega} V(\vec{r},\hbar\omega)G^{R}(\vec{r},E-\hbar\omega,\vec{r}',E') \end{aligned} \tag{2.20}$$

where $V(\vec{r},t)$ is represented by its Fourier transform components $\sum V(\vec{r},\hbar\omega)$. This perturbation term added to the RHS is the strength of the broadening due to interaction with the field [38]. This effect is included via a self-energy similar to the one used for contacts [34]. Under a first-order Born approximation, the solution to the equation of motion given by the modified Schrödinger equation in (2.20), is

$$\begin{aligned} G^{R}(\vec{r},E;\vec{r}',E') &= G_0^{R}(\vec{r},\vec{r}';E)\delta(E-E') \\ &+ \sum_{\omega}\int d\vec{r}''G_0^{R}(\vec{r},\vec{r}'';E)V(\vec{r}'',\hbar\omega)G_0^{R}(\vec{r}'',\vec{r}';E')\delta(E-\hbar\omega-E') \end{aligned} \tag{2.21}$$

In the presence of illumination, the current is obtained by substituting G^{R} in (2.19) by the expression in (2.21). The G^{R} can be computed numerically using the technique described in Chap. 7. However in the next section, we simplify (2.21) such that the illuminated characteristics can be predicted by an analytical extension of the DC $I(V)$ curve.

2.5.2 *Projecting Illuminated Characteristics from DC* I(V)

We propose two simplifications to the expression for G^{R} given in (2.21). The first is a uniform strength of interaction with the field over the device area ($V(\vec{r},\hbar\omega) = V(\hbar\omega)$). This is achieved by coupling an AC scalar potential through a gate electrode [39] or by applying the dipole approximation for a vector potential gauge [22]. The dipole approximation requires that the wavelength of the EM field be much larger than the size of the device. This condition is easily satisfied for a MIM diode, and for small geometric diodes. A further complication in geometric diodes is the field nonuniformity due to the shape of the conductor. For this, a field strength averaged over the geometry would serve as an initial correction.

The second approximation relates to the transport properties of electrons at energies separated by $\hbar\omega$. Here, we claim that the transport properties defined by G^{R} do not differ significantly for two energy levels spaced apart by $\hbar\omega$. The G^{R} for the two energies are similar if the photon energy is small compared to the energy of electrons. As the majority of conduction occurs due to electrons at the Fermi surface, the relevant energy for comparison is the Fermi energy ($\hbar\omega \ll E_{\mathrm{f}}$) measured with respect to the band edge. This assumption is similar to the nearly elastic scattering case considered by Datta [38]. The ramifications of this approximation are discussed at the end of the chapter.

Under these assumptions, (2.21) is simplified to

$$\begin{aligned} G^{\mathrm{R}}(\vec{r},E;\vec{r}',E') &= G_0^{\mathrm{R}}(\vec{r},\vec{r}';E)\delta(E-E') \\ &+ \sum_{\omega} V(\hbar\omega)\int d\vec{r}''G_0^{\mathrm{R}}(\vec{r},\vec{r}';E)\delta(E-\hbar\omega-E') \end{aligned} \tag{2.22}$$

where the Green's function in the integral is simplified under the assumption $E \approx E'$ as

$$G_0^{\mathrm{R}}(\vec{r},\vec{r}';E) = G_0^{\mathrm{R}}(\vec{r},\vec{r}'';E)G_0^{\mathrm{R}}(\vec{r}'',\vec{r}';E') \tag{2.23}$$

The spatial integral on the RHS of (2.22) leads to the volume of the device region (vol.) as there is no dependence on $\vec{r}''$ in the integrand. The Green's function under illumination then becomes

$$\begin{aligned} G^{\mathrm{R}}(\vec{r},E;\vec{r}',E') &= G_0^{\mathrm{R}}(\vec{r},\vec{r}';E)\delta(E-E') \\ &+ \mathrm{vol.}\sum_{\omega} V(\hbar\omega)G_0^{\mathrm{R}}(\vec{r},\vec{r}';E)\delta(E-\hbar\omega-E') \end{aligned} \tag{2.24}$$

Substituting the above expression in (2.19)

$$\begin{aligned} t_{21}(E,E') &\propto \left| G_0^{\mathrm{R}}(\vec{r},\vec{r}';E)\delta(E-E') + \mathrm{vol.}\sum_{\omega} V(\hbar\omega)G_0^{\mathrm{R}}(\vec{r},\vec{r}'E)\delta(E-\hbar\omega-E') \right|^2 \\ &= |G_0^{\mathrm{R}}(\vec{r},\vec{r}'E)|^2\delta^2(E-E') \\ &+ \left[G_0^{\mathrm{R}}(\vec{r},\vec{r}';E)\delta(E-E') + \left(\mathrm{vol.}\sum_{\omega} V(\hbar\omega)G_0^{\mathrm{R}}(\vec{r},\vec{r}';E)\delta(E-\hbar\omega-E') \right)^{cc} + \mathrm{cc} \right] \\ &+ \left| \mathrm{vol.}\sum_{\omega} V(\hbar\omega)G_0^{\mathrm{R}}(\vec{r},\vec{r}';E)\delta(E-\hbar\omega-E') \right|^2 \end{aligned} \tag{2.25}$$

where cc denotes complex conjugate. The term inside the square bracket has a product of two delta-functions $\delta(E - E')^*\delta(E - \hbar\omega - E')$, which is always zero. Also, in the third term, the square of the summation over delta-functions is equal to the summation of the squares as all cross terms with different ω are always zero due to the product of delta-functions $\delta(E - \hbar\omega_1 - E')^*\delta(E - \hbar\omega_2 - E')$. Therefore (2.25) reduces to

$$t_{21}(E,E') \propto |G_0^{\mathrm{R}}(\vec{r},\vec{r}';E)|^2\delta(E-E') + \mathrm{Vol}* \sum_{\omega}|V(\hbar\omega)|^2|G_0^{\mathrm{R}}(\vec{r},\vec{r}';E)|^2\delta(E-\hbar\omega-E') \tag{2.26}$$

The second term in the above equation represents a first-order, low-photon-energy correction to the Green's function for the un-illuminated case. This leads to the expression for illum given by

$$I_{\mathrm{illum}} = \frac{e\hbar^2}{T}\int dE\int dE'\int_{\vec{r}_2} d\vec{r}\int_{\vec{r}_1} d\vec{r}' \times \left[\begin{array}{l} \dfrac{|G_0^{\mathrm{R}}(\vec{r},\vec{r}';E)|^2\delta(E-E')}{4\pi^2\tau_\varphi(\vec{r},E)\tau_\varphi(\vec{r}',E')}f_1(E') - \dfrac{|G_0^{\mathrm{R}}(\vec{r}',\vec{r};E')|^2\delta(E'-E)}{4\pi^2\tau_\varphi(\vec{r},E)\tau_\varphi(\vec{r}',E')}f_2(E) \\ + \mathrm{vol.}^2\sum_{\omega}|V(\hbar\omega)|^2\left\{\begin{array}{l} \dfrac{|G_0^{\mathrm{R}}(\vec{r},\vec{r}';E)|^2\delta(E-\hbar\omega-E')}{4\pi^2\tau_\varphi(\vec{r},E)\tau_\varphi(\vec{r}',E')}f_1(E') \\ -\dfrac{|G_0^{\mathrm{R}}(\vec{r}',\vec{r};E)|^2\delta(E'-\hbar\omega-E)}{4\pi^2\tau_\varphi(\vec{r},E)\tau_\varphi(\vec{r}',E')}f_2(E) \end{array}\right\} \end{array}\right] \tag{2.27}$$

We now perform the integral with respect to E' in (2.27) using the sifting property of the delta function. Under the condition $\hbar\omega \ll E_{\mathrm{f}}$, we also approximate that τ_φ does not vary significantly from E to $E + \hbar\omega$. The validity of this is in-line with the approximation made for G^{R} in that the interaction of an electron with the reservoirs is similar at two closely spaced energies. With this simplification, the illum is given by

$$I_{\mathrm{illum}} = \frac{e\hbar^2}{T}\int dE\int_{\vec{r}_2} d\vec{r}\int_{\vec{r}_1} d\vec{r}' \times \left[\begin{array}{l} \dfrac{|G_0^{\mathrm{R}}(\vec{r},\vec{r}';E)|^2}{4\pi^2\tau_\varphi(\vec{r},E)\tau_\varphi(\vec{r}',E)}f_1(E) - \dfrac{|G_0^{\mathrm{R}}(\vec{r}',\vec{r};E')|^2}{4\pi^2\tau_\varphi(\vec{r},E)\tau_\varphi(\vec{r}',E)}f_2(E) \\ + \mathrm{vol.}^2\sum_{\omega}|V(\hbar\omega)|^2\left\{\begin{array}{l} \dfrac{|G_0^{\mathrm{R}}(\vec{r},\vec{r}';E)|^2}{4\pi^2\tau_\varphi(\vec{r},E)\tau_\varphi(\vec{r}',E)}f_1(E-\hbar\omega) \\ -\dfrac{|G_0^{\mathrm{R}}(\vec{r}',\vec{r};E)|^2\delta(E'-\hbar\omega-E)}{4\pi^2\tau_\varphi(\vec{r},E)\tau_\varphi(\vec{r}',E')}f_2(E) \end{array}\right\} \end{array}\right] \tag{2.28}$$

which can be simplified to

$$
\begin{aligned}
I_{\text{illum}} &= \tfrac{e\hbar^2}{T} \int dE \int_{\vec{r}_2} d\vec{r} \int_{\vec{r}_1} d\vec{r}' \\
&\times \left[\begin{array}{l} \dfrac{|G_0^{\mathrm{R}}(\vec{r},\vec{r}';E)|^2}{4\pi^2 \tau_\varphi(\vec{r},E)\tau_\varphi(\vec{r}',E)} \{f_1(E) - f_2(E)\} \\ \\ + \text{vol.}^2 \displaystyle\sum_\omega |V(\hbar\omega)|^2 \dfrac{|G_0^{\mathrm{R}}(\vec{r},\vec{r}';E)|^2}{4\pi^2 \tau_\varphi(\vec{r},E)\tau_\varphi(\vec{r}',E)} \{f_1(E-\hbar\omega) - f_2(E)\} \end{array} \right]
\end{aligned} \tag{2.29}
$$

The second term in the above equation that represents the additional current due to illumination and can be written in terms of the un-illuminated (dark) current given by the first term. This is done by combining the $\hbar\omega$ with the DC voltage applied between the two contacts (V_{D}). Assuming that contact 2 is the ground, (2.29) can be written in terms of the Fermi distribution $f(E) = [1 + \exp((E - E_{\mathrm{f}})/kT)]^{-1}$ as

$$
\begin{aligned}
I_{\text{illum}} &= \tfrac{e\hbar^2}{T} \int dE \int_{\vec{r}_2} d\vec{r} \int_{\vec{r}_1} d\vec{r}' \\
&\times \left[\begin{array}{l} \dfrac{|G_0^{\mathrm{R}}(\vec{r},\vec{r}';E)|^2}{4\pi^2 \tau_\varphi(\vec{r},E)\tau_\varphi(\vec{r}',E)} \{f(E - eV_{\mathrm{D}}) - f(E)\} \\ \\ + \mathit{vol.}^2 \displaystyle\sum_\omega |V(\hbar\omega)|^2 \dfrac{|G_0^{\mathrm{R}}(\vec{r},\vec{r}';E)|^2}{4\pi^2 \tau_\varphi(\vec{r},E)\tau_\varphi(\vec{r}',E)} \{f(E - (eV_{\mathrm{D}} + \hbar\omega)) - f(E)\} \end{array} \right]
\end{aligned} \tag{2.30}
$$

This can be interpreted as

$$
I_{\text{illum}}(V_{\mathrm{D}}) = I_{\text{dark}}(V_{\mathrm{D}}) + \text{vol.}^2 \sum_\omega |V(\hbar\omega)|^2 I_{\text{dark}}\left(V_{\mathrm{D}} + \frac{\hbar\omega}{e}\right) \tag{2.31}
$$

2.5.3 Discussion

Equation (2.31) allows an analytical evaluation of the illuminated characteristics from a dark $I(V)$ curve, similar to the first-order approximation of (2.6) depicted graphically using a piecewise linear dark $I(V)$ curve in Fig. 2.8. Although the equation for an MIM diode was derived for a single-frequency illumination, its multispectral extension also consists of an integral over the contribution from different frequencies [24].

In analogy with the high-frequency operating mechanism described for an MIM diode in Fig. 2.2, (2.31) indicates that the interaction of the electrons in the device region is equivalent to the modulation of electron energies in the contact. This simplified picture for the interaction emerges because the electronic transport properties are assumed to be constant in a narrow range of energies given by the additional photon energy ($\hbar\omega$) acquired by the electrons in the device region. The derivation presented here essentially transferred the electron interaction with the photon from the device region to the contacts.

The assumption of $\hbar\omega \ll E_{\mathrm{f}}$ is the most significant consideration of the derivation. Earlier, we stated this condition without analyzing its physical significance. Transport properties, e.g., tunneling probability in an MIM diode, can be a strong function of energy. However, in the case of MIM diodes the photon–electron interaction occurs only in the contacts due to the absence of electrons in the insulator. This is the basis for the semiclassical theory described in Sect. 2.2. In a mesoscopic junction like the geometric diode, due to the absence of an energy barrier the transmission is a weaker function of energy than in MIM diodes. Therefore, in narrow energy ranges, the assumption of constant transport behavior has greater validity. Ultimately, the effect of the added photon energy is relative to the existing electron-energy. If this energy is large, such that the transmission is highly likely, the change in transmission by adding photon energy will be small. A measure of validity for the existing electron energy is the Fermi level and hence the condition $\hbar\omega \ll E_{\mathrm{f}}$.

A final point of discussion concerns the material for the thin-film used in the device region. Equation (2.31) is applicable under the assumption that the photon energy (E_{ph}) is small compared to the Fermi level (E_{f}). This depends on the value of the E_{f}. For metals, E_{f} is on the order of a few electron-volts so that the result holds even at far-to-mid-infrared. However, for a material like graphene, the E_{f} is closer to zero, but can be varied by applying a gate-voltage or by doping.

In summary, we have shown that the $I(V)$ characteristics for a general mesoscopic junction can be described by a formalism similar to that used for MIM diodes, within the limits of some assumptions. Therefore the optical frequency rectification analysis that was presented in this chapter applies not just to MIM diodes but also to a wider range of optical frequency rectifiers.

References

1. Grover S. Diodes for optical rectennas. PhD Thesis, University of Colorado, Boulder; 2011.
2. Brown WC. Optimization of the efficiency and other properties of the rectenna element. 1976. p. 142–4.
3. Shinohara N, Matsumoto H. Experimental study of large rectenna array for microwave energy transmission. IEEE Trans Microw Theory Tech. 1998;46(3):261–8.
4. Hagerty JA, Helmbrecht FB, McCalpin WH, Zane R, Popovic ZB. Recycling ambient microwave energy with broad-band rectenna arrays. IEEE Trans Microw Theory Tech. 2004;52(3):1014–24.
5. Singh P, Kaneria S, Anugonda VS, Chen HM, Wang XQ, et al. Prototype silicon micropower supply for sensors. IEEE Sens J. 2006;6(1):211–22.
6. Fumeaux C, Herrmann W, Kneubühl FK, Rothuizen H. Nanometer thin-film Ni-NiO-Ni diodes for detection and mixing of 30 THz radiation. Infrared Phys Technol. 1998;39 (3):123–83.

7. Bailey RL. A proposed new concept for a solar-energy converter. J Eng Power. 1972;94(2):73–77.
8. Marks AM. Device for conversion of light power to electric power. US Patent No. 4445050; 1984.
9. Berland B. Photovoltaic technologies beyond the horizon: optical rectenna solar cell, NREL report no. SR-520-33263, final report; 2003.
10. Grover S, Joshi S, Moddel G. Theory of operation for rectenna solar cells. J Phys D. 2013.
11. Grover S, Moddel G. Applicability of metal/insulator/metal (MIM) diodes to solar rectennas. IEEE J Photovoltaics. 2011;1(1):78–83.
12. Sedra AS, Smith KC. Microelectronic circuits. 4th ed. New York: Oxford University Press; 1997.
13. Yoo T, Chang K. Theoretical and experimental development of 10 and 35 GHz rectennas. IEEE Trans Microw Theory Tech. 1992;40(6):1259–66.
14. Brown ER. A system-level analysis of Schottky diodes for incoherent THz imaging arrays. Solid State Electron. Mar 2004;48:2051–3.
15. Kazemi H, Shinohara K, Nagy G, Ha W, Lail B, et al. First THz and IR characterization of nanometer-scaled antenna-coupled InGaAs/InP Schottky-diode detectors for room temperature infrared imaging. Infrared Technol Appl XXXIII. 2007;6542(1):65421.
16. Hübers H-W, Schwaab GW, Röser HP. Video detection and mixing performance of GaAs Schottky-barrier diodes at 30 THz and comparison with metal-insulator-metal diodes, J Appl Phys. 1994;75(8):4243–8.
17. Hartman TE. Tunneling of a wave packet. J Appl Phys. Dec 1962;33(12):3427–33.
18. Nagae M. Response time of metal-insulator-metal tunnel junctions. Jpn J Appl Phys. 1972;11 (11):1611–21.
19. Rockwell S, Lim D, Bosco BA, Baker JH, Eliasson B, et al. Characterization and modeling of metal/double-insulator/metal diodes for millimeter wave wireless receiver applications. In Radio frequency integrated circuits (RFIC) symposium, IEEE, Honolulu, HI; 2007. p. 171–4.
20. Sanchez A, Davis CF, Liu KC, Javan A. The MOM tunneling diode: theoretical estimate of its performance at microwave and infrared frequencies. J Appl Phys. 1978;49(10):5270–7.
21. Grover S, Dmitriyeva O, Estes MJ, Moddel G. Traveling-wave metal/insulator/metal diodes for improved infrared bandwidth and efficiency of antenna-coupled rectifiers. IEEE Trans Nanotechnol. 2010;9(6):716–22.
22. Eliasson BJ. Metal-insulator-metal diodes for solar energy conversion. PhD Thesis, University of Colorado at Boulder, Boulder; 2001.
23. Tien PK, Gordon JP. Multiphoton process observed in the interaction of microwave fields with the tunneling between superconductor films. Phys Rev. 1963;129(2):647–51.
24. Tucker JR, Feldman MJ. Quantum detection at millimeter wavelengths. Rev Mod Phys. 1985;57(4):1055–113.
25. Tucker JR. Quantum limited detection in tunnel junction mixers. IEEE J Quantum Electron. 1979;QE-15(11):1234–58.
26. Michael Kale B. Electron tunneling devices in optics, Opt Eng. 1985;24(2):267–74.
27. Wilke I, Oppliger Y, Herrmann W, Kneubühl FK. Nanometer thin-film Ni-NiO-Ni diodes for 30 THz radiation. Appl Phys Mater Sci Process. Apr 1994;58(4):329–41.
28. Hobbs PC, Laibowitz RB, Libsch FR, LaBianca NC, Chiniwalla PP. Efficient waveguide-integrated tunnel junction detectors at 1.6 μm, Opt Express. 2007;15 (25):16376–89.
29. Estes MJ, Moddel G. Surface plasmon devices. US Patent 7,010,183; 2006.
30. Fal'ko V. Nonlinear properties of mesoscopic junctions under high-frequency field irradiation. Europhys Lett. 1989;8(8):785–9.
31. Datta S. Steady-state transport in mesoscopic systems illuminated by alternating fields. Phys Rev B. 1992;45(23):13761–4.
32. Liu J, Giordano N. Nonlinear response of a mesoscopic system. Phys B. 1990;165&166:279–80.
33. Platero G, Aguado R. Photon-assisted transport in semiconductor nanostructures. Phys Rep. 2004;395(1–2):1–157.

34. Kienle D, Vaidyanathan M, Léonard F. Self-consistent ac quantum transport using nonequilibrium Green functions. Phys Rev B. 2010;81:115455.
35. Datta S, Anantram MP. Steady-state transport in mesoscopic systems illuminated by alternating fields. Phys Rev B. 1992;45(23):13761–4.
36. Landauer R. Johnson-Nyquist noise derived from quantum mechanical transmission. Phys D. 1989;38:226–9.
37. Ferry DK, Goodnick SM, Bird J. Transport in nanostructures. 2nd ed. Cambridge: Cambridge University Press; 2009.
38. Datta S. Quantum transport: atom to transistor. Cambridge: Cambridge University Press; 2005.
39. Pedersen MH, Büttiker M. Scattering theory of photon-assisted electron transport. Phys Rev B. 1998;58(19):12993–3006.
40. Dagenais M, Choi K, Yesilkoy F, Chryssis AN, Peckerar MC. Solar spectrum rectification using nano-antennas and tunneling diodes. Proc SPIE. 2010;7605:76050E–1.